Journal of Power Sources 185 (2008) 765–775

Contents lists available at ScienceDirect

Journal of Power Sources

journal homepage: www.elsevier.com/locate/jpowsour

Modelling of coupled electron and mass transport in anisotropic proton-exchange membrane fuel cell electrodes

W.W. Yang[a], T.S. Zhao[a,*], Y.L. He[b]

[a] Department of Mechanical Engineering, The Hong Kong University of Science and Technology, Clear Water Bay, Kowloon, Hong Kong, China
[b] School of Energy and Power Engineering, Xi'an Jiaotong University, Xi'an 710049, China

ARTICLE INFO

Article history:
Received 1 May 2008
Received in revised form 5 May 2008
Accepted 30 June 2008
Available online 31 July 2008

Keywords:
Proton-exchange membrane fuel cell
Two-phase mass transport
Anisotropy
Deformation
Gas-diffusion layer

ABSTRACT

As one of the key components of proton-exchange membrane fuel cells, the gas-diffusion layer (GDL) that is made of carbon fibres usually exhibits strong structural anisotropy. Nevertheless, the GDL has traditionally been simplified as a homogeneous porous structure in modelling the transport of species through the GDL. In this work, a coupled electron and two-phase mass transport model for anisotropic GDLs is developed. The effects of anisotropic GDL transport properties due to the inherent anisotropic carbon fibres and caused by GDL deformations are studied. Results indicate that the inherent structural anisotropy of the GDL significantly influences the local distribution of both cathode potential and current density. Simulation results further indicate that a GDL with deformation results in an increase in the concentration polarization due to the increased mass-transfer resistance in the deformed GDL. On the other hand, the ohmic polarization is found to be smaller in the deformed GDL as the result of the decreased interfacial contact resistance and electronic resistance in the GDL. This result implies that an optimum deformation needs to be achieved so that both concentration and ohmic losses can be minimized.

1. Introduction

The proton-exchange membrane fuel cell (PEMFC) is regarded as an alternative power source for electric vehicles by the virtue of its high-energy efficiency, pollution-free characteristics, as well as the simplicity in its design and operation. It has received more and more attention over the past decade. In order to achieve a better performance, it is essential to have a deep understanding of the physicochemical phenomena occurring in each component of the cell.

As one of the key components, the gas-diffusion layer (GDL), usually made of highly porous material such as carbon fibre papers or cloths, serves to facilitate the distribution of reactants and removal of by-products, and to provide the path for electrons as well as heat transport. Since GDLs are typically made of fibrous porous materials they exhibit strong structural anisotropy due to the special constitutive orientations of carbon fibres. This intrinsic anisotropy of the GDL consequently leads to different transport properties in the through-plane and in-plane directions. Among the existing PEMFC models reported in the literature however, only a few [1–4] consider the effect of the inherent anisotropy of the GDL. Zhou and Liu [1] numerically studied the effect of the electrical resistance in the GDL on the current distribution as well as on the cell performance. In that work, the anisotropic characteristics of the GDL were evaluated by using different electrical conductivities in the through-plane and in-plane directions. Pasaogullari et al. [2] presented a two-dimensional model to investigate the effects of the anisotropic properties on the coupled heat and water transport in the GDL. Their results indicated that the inherent anisotropy of the GDL plays an important role in determining the temperature distribution in the GDL. Recently, Pharoah et al. [3] briefly reviewed the approaches currently employed to define the effective transport coefficients in the GDL. They also developed a two-dimensional single-phase model to examine the effect of the inherent anisotropy of the GDL on the profile of the local current density and the cell performance. Although both the isotropic model and the anisotropic models gave nearly identical polarization curves for certain sets of parameters, the profiles of local current density are quite different. More recently, a simplified method was also developed by Meng [4] for solving the anisotropic transport problem in a PEMFC.

In addition to the inherent anisotropy, the GDL usually undergoes deformation when all the cell components are assembled. This deformation causes significant changes in the physical properties of the GDL and their distributions. Since the GDL tends to have a larger deformation under the rib region than under the channel region, inevitably, the local properties of the GDL show strongly

* Corresponding author. Tel.: +852 2358 8647; fax: +852 2358 1543.
E-mail address: metzhao@ust.hk (T.S. Zhao).

0378-7753/$ – see front matter © 2008 Elsevier B.V. All rights reserved.
doi:10.1016/j.jpowsour.2008.06.100

Nomenclature

A_v	specific area (m^{-1})
C	molar concentration ($mol\ m^{-3}$)
D	diffusivity ($m^2\ s^{-1}$)
F	Faraday constant (96 478 $C\ mol^{-1}$)
i_0	exchange current density ($A\ m^{-3}$)
i_+	proton current vector ($A\ m^{-2}$)
I	current density ($A\ m^{-2}$)
j_c	cathodic current density ($A\ m^{-3}$)
j_p	source term in proton conservation equation ($A\ m^{-3}$)
j_s	source term in electron conservation equation ($A\ m^{-3}$)
k_c	condensation rate (s^{-1})
k_e	evaporation rate ($atm^{-1}\ s^{-1}$)
k_H	Henry's law constant
k_r	relative permeability
K	permeability of porous material (m^2)
L	thickness of porous layers (m)
$\dot{m}$	source term in mass conservation equation ($kg\ m^{-3}\ s^{-1}$)
m_{Pt}	Pt loading in cathode catalyst layer ($kg\ m^{-2}$)
M	molecular weight ($kg\ mol^{-1}$)
n_d	electro-osmotic drag coefficient
N	mol flux ($mol\ m^{-2}\ s^{-1}$)
p_c	capillary pressure (Pa)
p_g	gas-phase pressure (Pa)
p_l	liquid-phase pressure (Pa)
R	gas constant or radius ($J\ mol^{-1}\ K^{-1}$) or (m)
$\dot{R}$	source term in species conservation equation ($mol\ m^{-3}\ s^{-1}$)
$\tilde{R}$	interfacial species transfer rate ($mol\ m^{-3}\ s^{-1}$)
R_{cunt}	interfacial contact resistance ($\Omega\ m^2$)
s	liquid saturation
T	temperature (K)
U_0	thermodynamic equilibrium voltage of ORR (V)
V_c	cathode voltage (V)
x	coordinate (m), or mole fraction in liquid solution ($mol\ mol^{-1}$)
y	coordinate (m), or mole fraction in gas mixture ($mol\ mol^{-1}$)

Greek letters

α_c	charge-transfer coefficient at cathode
δ	thickness of Nafion film (m)
ε	porosity of porous medium
η	overpotential (V)
θ_c	contact angle (°)
μ	viscosity ($kg\ m^{-1}\ s^{-1}$)
ρ	density ($kg\ m^{-3}$)
σ	interfacial tension ($N\ m^{-1}$)
σ_e	ionic conductivity of membrane ($\Omega^{-1}\ m^{-1}$)
σ_s	electrical conductivity ($\Omega^{-1}\ m^{-1}$)

Subscripts

c	cathode
cl	catalyst layer
g	gas phase
gdl	gas diffusion layer
in	inlet condition
in-p	in-plane direction
l	liquid phase
mem	membrane
N	Nafion phase
th-p	through-plane direction
W	water
WV	water vapour

Superscripts

eff	effective value
ref	reference value
sat	saturated value

inhomogeneous distributions along the in-plane direction. In addition, the interfacial contact resistance is also changed, which is known as one of the important parameters that affects the voltage loss in a PEMFC. Experimental studies [5–8] have been conducted to examine the effect of the deformation on the physical properties of the GDL, such as porosity, electrical/thermal conductivity and permeability, as well as interfacial contact resistance. The effect of the GDL deformation on the performance of a PEMFC has also been experimentally investigated [9,10]. To date, few models have been reported to examine the effect of GDL deformation. Zhou et al. [11,12] numerically studied the effect of the GDL deformation on the performance of a PEMFC. Although the influence of GDL deformation on the contact resistance and porosity distribution were taken into account in their models, the impact on electrical resistance in the GDL was not considered. Furthermore, the anisotropic nature of the GDL was neglected in their model. Hottinen et al. [13] numerically studied the influence of GDL deformation on the profiles of local current density by using a single-phase model. Although the anisotropic properties of the GDL such as electronic conductivity and permeability were taken into account, the anisotropic diffusion coefficients of oxygen transport in the GDL was not indicated. More recently, Hottinen et al. [14] studied the effect of the GDL deformation on the temperature distribution in a PEMFC.

The above review of the literature indicates that there is still a lack of a sound mathematical model that can take into account the influences of both the intrinsic GDL anisotropy associated with carbon fibres and the structural GDL anisotropy caused by inhomogeneous GDL deformation. The objective of the work is to develop a 2D model that can simulate coupled electron and two-phase mass transport in a PEMFC cathode. With this model, we numerically have studied the effects of anisotropic GDL properties associated with carbon fibres and caused by GDL deformation on the distributions of reactant, potential, overpotential and the current density as well as on the cell performance.

2. Formulation

Consider the physical domain sketched in Fig. 1, which consists of a cathode GDL, a cathode catalyst layer (CL) and a polymer electrolyte membrane (PEM). Note that since both channel width and rib width in a parallel flow-field are symmetrical with respect to their middle points, only a half-rib width and a half-channel width need to be considered to save the computing time. The mass transport of gas oxygen and water vapour in the GDL are governed by the general convection-diffusion transport equation, i.e.

$$\frac{\partial}{\partial x}(u_g C_{i,g}) + \frac{\partial}{\partial y}(v_g C_{i,g}) - \frac{\partial}{\partial x}\left(D^{eff}_{i,g,x}\frac{\partial C_{i,g}}{\partial x}\right) - \frac{\partial}{\partial y}\left(D^{eff}_{i,g,y}\frac{\partial C_{i,g}}{\partial y}\right) = \dot{R}_i, \quad i: O_2, WV \tag{1}$$

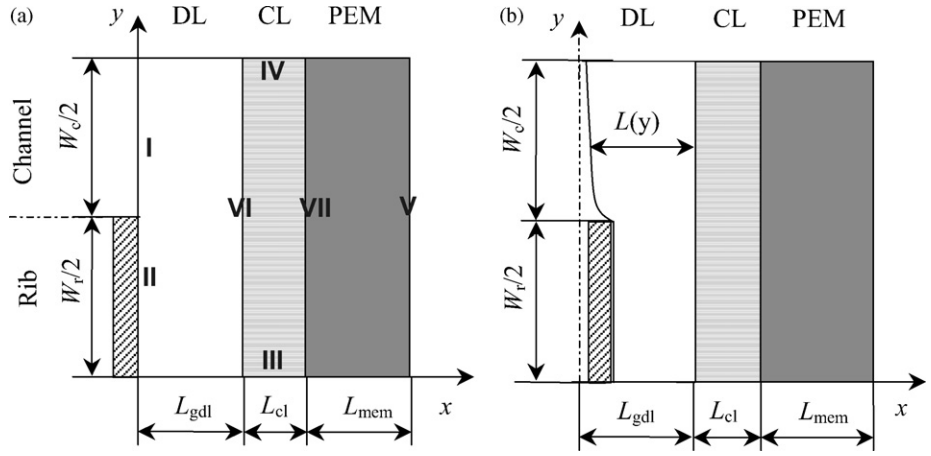

Fig. 1. Modelling domain: (a) geometry of the GDL without deformation; (b) geometry of the GDL with deformation. Roman numerals refer to boundaries of modelled geometries.

where $D_{i,g}^{eff}$ is the effective diffusion coefficient of species in a porous medium. For a porous structure that is made of random fibrous materials, like GDLs, $D_{i,g}^{eff}$ is given by [15,16]

$$D_{i,g}^{eff} = D_{i,g}^{0} f(\varepsilon) g(s) = D_{i,g}^{0} \varepsilon \left(\frac{\varepsilon - 0.11}{1 - 0.11} \right)^{\alpha} (1-s)^{\beta} \tag{2}$$

where the constant α is 0.521 and 0.785 for the in-plane and through-plane diffusions, respectively. The constant β is set to be 1.5 for both types of diffusion. In the CL, the effective diffusion coefficient of a given species can be obtained from the Bruggeman correlation:

$$D_{i,g}^{eff} = D_{i,g}^{0} \varepsilon^{1.5} (1-s)^{\beta} \tag{3}$$

In Eq. (1), u_g and v_g represent the superficial velocities of gas mixture in a porous medium, that can be calculated by Darcy's law if the pressure field is available. The gas pressure can be obtained by solving

$$\frac{\partial}{\partial x}\left(-\rho_g \frac{K k_{rg}}{\mu_g} \frac{\partial p_g}{\partial x} \right) + \frac{\partial}{\partial y}\left(-\rho_g \frac{K k_{rg}}{\mu_g} \frac{\partial p_g}{\partial y} \right) = \dot{m}_g \tag{4}$$

The liquid saturation distribution in the cathode porous region, s, can be modelled by

$$\frac{\partial}{\partial x}\left[\left(-\frac{\rho_l K k_{rl}}{\mu_l} \right) \left(-\frac{dp_c}{ds} \frac{\partial s_l}{\partial x} + \frac{\partial p_g}{\partial x} \right) \right] + \frac{\partial}{\partial y}\left[\left(-\frac{\rho_l K k_{rl}}{\mu_l} \right) \left(-\frac{dp_c}{ds} \frac{\partial s_l}{\partial y} + \frac{\partial p_g}{\partial y} \right) \right] = \dot{m}_l \tag{5}$$

where p_c is the capillary pressure, which represents the difference between the gas pressure and liquid pressure as follows:

$$p_c = p_g - p_l = \sigma \cos\theta_c \left(\frac{\varepsilon}{K} \right)^{0.5} J(s) \tag{6}$$

In order to account for the effect of water evaporation and condensation, the interfacial transfer rate of water between the liquid and gas phase is given by [17]

$$\tilde{R}_w = \begin{cases} k_e \dfrac{\varepsilon s_l \rho_l}{M_{H_2O}} (y_{WV} p_g - p_{WV}^{sat}), & y_{WV} p_g < p_{WV}^{sat} \\ k_c \dfrac{\varepsilon (1-s_l) y_{WV}}{RT} (y_{WV} p_g - p_{WV}^{sat}), & y_{WV} p_g > p_{WV}^{sat} \end{cases} \tag{7}$$

where p_{WV}^{sat} and y_{WV} denote the saturation pressure of water vapour and the mole fraction of water vapour in the cathode gas phase, respectively. Note that the interfacial transfer of water between the phases is embodied in the source terms on the right-hand sides of Eqs. (4) and (5).

With respect to the dissolved water in the membrane, water transfer is driven by the concentration gradient and electro-osmotic drag. The general conservation of dissolved water in the membrane can be expressed by

$$\frac{\partial}{\partial x}\left(\frac{i_+}{F} n_d \right) + \frac{\partial}{\partial y}\left(\frac{i_+}{F} n_d \right) - \frac{\partial}{\partial x}\left(D_{W,N} \frac{\partial C_{W,N}}{\partial x} \right) - \frac{\partial}{\partial y}\left(D_{W,N} \frac{\partial C_{W,N}}{\partial y} \right) = 0 \tag{8}$$

where the electro-osmotic drag (EOD) coefficient, n_d, and the diffusivity of water in the membrane, $D_{W,N}$, are both functions of the water content in the membrane.

In addition to the two-phase mass transport processes in the porous cathode, the transport of electrons through the catalyst layer and gas-diffusion layers and the transport of protons through the membrane phase must also be considered. The governing equations that describe the transport of electrons and protons in the membrane phase are, respectively, given by

$$\frac{\partial}{\partial x}\left(\sigma_{s,x} \frac{\partial \phi_s}{\partial x} \right) + \frac{\partial}{\partial y}\left(\sigma_{s,y} \frac{\partial \phi_s}{\partial y} \right) = j_s \tag{9}$$

and

$$\frac{\partial}{\partial x}\left(\sigma_{e,x} \frac{\partial \phi_e}{\partial x} \right) + \frac{\partial}{\partial y}\left(\sigma_{e,y} \frac{\partial \phi_e}{\partial y} \right) = j_p \tag{10}$$

where σ_s is the electrical conductivity of the electron-conducting phase, while σ_e is the proton conductivity in the membrane, which is known as to be a function of water content in the membrane.

Up to this point, we have presented all the governing equations that describe two-phase mass transport and charge transport in the PEMFC cathode. To make the above governing equations closed, some constitutive correlations and definitions are needed. These include capillary pressure, relative permeability for both phases, sources terms, and so on. All these correlations and associated nomenclatures are listed in Table 1.

2.1. Boundary conditions

As indicated in Fig. 1, there are seven boundaries specified in the modelling domain as marked with Roman numerals. The conditions at each boundary are described below.

Table 1
Constitutive correlations and definitions

Parameters	Expressions
Capillary pressure	$p_c = p_g - p_l = \sigma\cos\theta_c(\varepsilon/K)^{0.5}J(s), J(s) = \begin{cases} 1.417(1-s) - 2.120(1-s)^2 + 1.263(1-s)^3, & 0 < \theta_c \le 90^\circ \\ 1.417s - 2.120s^2 + 1.263s^3, & 90^\circ < \theta_c < 180^\circ \end{cases}$
Relative permeabilities	$k_{rl} = s^3$ liquid; $k_{rg} = (1-s)^3$ gas
General generation rate of mass in liquid phase	$\dot{m}_l = \begin{cases} -M_{H_2O}\tilde{R}_w & \text{GDL} \\ M_{H_2O}\frac{j_c}{2F} + M_{H_2O}\frac{N_{W,cross}}{L_{CL}} - M_{H_2O}\tilde{R}_w & \text{CL} \end{cases}$
General generation rate of mass in gas phase	$\dot{m}_g = \begin{cases} M_{H_2O}\tilde{R}_w & \text{GDL} \\ -M_{O_2}\frac{j_c}{4F} + M_{H_2O}\tilde{R}_w & \text{CL} \end{cases}$
Mole generation rate of species	$\dot{R}_{O_2} = \begin{cases} 0 \\ -\frac{j_c}{4F} \end{cases}$, $\dot{R}_{WV,c} = \begin{cases} \tilde{R}_w & \text{GDL} \\ \tilde{R}_w & \text{CL} \end{cases}$
General generation rate of charges	$j_p = \begin{cases} 0 & \text{MEM} \\ -j_c & \text{CL} \end{cases}$, $j_s = \begin{cases} 0 & \text{GDL} \\ j_c & \text{CL} \end{cases}$
Thickness of the GDL under inhomogeneous compression [5]	$L(y) = \begin{cases} L_{comp} \\ 19.30314\log((y-0.0005)\times 10^6 + 1)\times 10^{-6} + L_{comp} \end{cases}$, L_{comp}: thickness of GDL under the rib (L_{comp} = 250 μm)
Porosity of the GDL under inhomogeneous compression [5]	$\varepsilon(y) = \varepsilon_0\frac{L(y)-L_{min}}{L_{gdl}-L_{min}}$, $L_{min} = (1-\varepsilon_0)L_{gdl}$
Electrical conductivity of the GDL [5]	$\sigma_{in\text{-}p}(y) = 6896 - 1.159\times 10^7\,L(y)$, $\sigma_{th\text{-}p}(y) = 3285 - 8.385\times 10^6\,L(y)$
Interfacial contact resistance [5]	$R_{cont}(y) = 5.83\times 10^{-10}\exp[2.06\times 10^4\,L(y)]$

Boundary I. This boundary represents the inlet of the reactant supply in the cathode, at which the concentration of gas species, gas phase pressure, and liquid water saturation are all specified to be inlet conditions. With respect to the electrical potential, the gradient is set to be zero at the direction normal to this boundary:

$$C_{O_2,g} = C_{O_2,in}, \quad C_{WV,g} = C_{WV,in}, \quad p_g = p_{g,in}, \quad s = s_{in},$$
$$\nabla\phi_s|_{\text{normal to I}} = 0 \tag{11}$$

Boundary II. This boundary is the interface between the GDL and the rib collector, which is an impermeable wall to mass/species transfer. Accordingly, the flux of the gaseous species and liquid species in the *x* direction (normal to boundary II) are specified to be zero. At this interface, the electrical potential is set to be the applied potential, i.e.

$$\frac{\partial C_{O_2,g}}{\partial x} = 0, \quad \frac{\partial C_{WV,g}}{\partial x} = 0, \quad \frac{\partial p_g}{\partial x} = 0, \quad \frac{\partial s}{\partial x} = 0, \quad \phi_s = V_c \tag{12}$$

Boundaries III and IV. These two boundaries are symmetrical to the middle point of rib width and the middle point of channel width, respectively. Hence, the gradients of all the variables in *x* direction are set to zero:

$$\frac{\partial C_{O_2,g}}{\partial y} = 0, \quad \frac{\partial C_{WV,g}}{\partial y} = 0, \quad \frac{\partial p_g}{\partial y} = 0, \quad \frac{\partial s}{\partial y} = 0, \quad \frac{\partial C_{W,N}}{\partial y} = 0,$$
$$\frac{\partial \phi_s}{\partial y} = 0, \quad \frac{\partial \phi_e}{\partial y} = 0 \tag{13}$$

Boundary V. This boundary represents the interface between the membrane and the anode. At this boundary, it is assumed that the water concentration is only a function of the water vapour activity in the anode gas stream and an equilibrium condition is reached between this water vapour and the dissolved water in the membrane. As for the ionic potential, the latter is set to zero as a reference at this boundary:

$$C_{W,N} = C^{eq}_{W,N,a}, \quad \phi_e = 0 \tag{14}$$

The equilibrium water concentration when the membrane is only in contact with water vapour [18] is obtained from

$$C^{eq}_{W,N} = C_f(0.043 + 17.81a_w - 39.85a_w^2 + 36.0a_w^3) \tag{15}$$

where a_w represents the water vapour activity ($a_w = x_{vapor}p_{g,a}/p^{sat}_{vapor}$).

Boundary VI. This boundary represents the interface between the GDL and the CL. The electrical current and the fluxes of oxygen, vapour and liquid water are continuous at this interface to satisfy the general mass/species/charge balance. Since there is no ionic phase in the GDL, the flux of protons is set to be zero at this

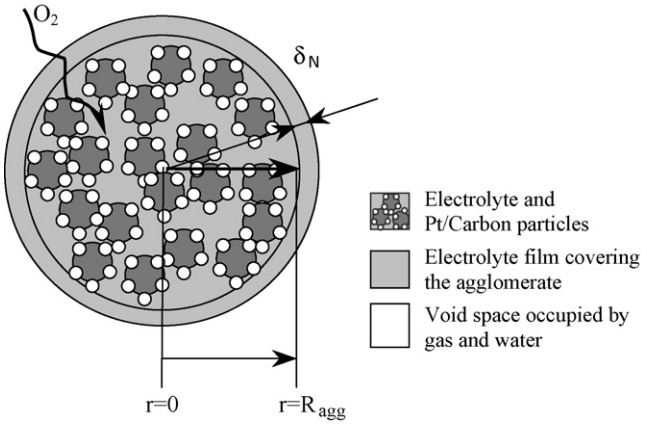

Fig. 2. Schematic of agglomerate structure in cathode catalyst layer.

Table 2
Correction factors and correlations in thin film-agglomerate model

Parameters, symbols	Expressions
Correction factor, ξ_1	$\xi_1 = \frac{1}{1+[(\delta_N/(\delta_N+R_{agg}))](D^{eff}_{O_2,agg}/D_{O_2,N})[\phi R_{agg}\coth(\phi R_{agg})-1]}$
Correction factor, ξ_2	$\xi_2 = \frac{3}{(\phi R_{agg})^2}[\phi R_{agg}\ \coth(\phi R_{agg}) - 1]$
Correction factor, ξ_3 [21]	$\xi_3 = 1 - s$
The Thiele modulus, ϕR_{agg}	$\phi R_{agg} = \sqrt{\frac{A_{agg}j^{ref}_{0,O_2}}{nFD^{eff}_{O_2,agg}C^{ref}_{O_2}}}\exp\left(\frac{\alpha_c F}{2RT}\eta_c\right)R_{agg}$
Effective specific area in agglomerate, A_{agg}	$A_{agg} = \frac{A}{\varepsilon_s+\varepsilon_{N,agg}(\varepsilon_s/(1-\varepsilon_{N,agg}))}$
Effective diffusion coefficient of oxygen, $D^{eff}_{O_3,agg}$	$D^{eff}_{O_2,agg} = D_{O_2,N}\varepsilon^{1.5}_{N,agg}$

Table 3
Cell geometric dimensions and operating conditions

Parameters	Symbols	Value	Unit
Thicknesses of functional layers	L_{gdl}, L_{cl}, L_{mem}	0.38, 0.02, 0.05	mm
Width of channel, rib	w_c, w_r	1.0, 1.0	mm
Operation temperature	T	348.15	K
Inlet pressure of cathode	$p_{g,in}$	1.013×10^5	Pa
Inlet oxygen concentration	$C_{O_2,in}$	7.35	mol m^{-3}
Inlet water vapour concentration	$C_{WV,in}$	0	mol m^{-3}
Inlet liquid saturation of cathode	$s_{c,in}$	0	–
Relative humidity of anode	RH	100%	–

boundary:

$$N_i|_- = N_i|_+, \quad i: \mathrm{O_2,WV,W}, \qquad \sigma_s \frac{\partial \phi_s}{\partial x}\bigg|_- = \sigma_s \frac{\partial \phi_s}{\partial x}\bigg|_+, \qquad \frac{\partial \phi_e}{\partial x} = 0 \tag{16}$$

Boundary VII. This boundary represents the interface between the CL and the PEM. At this interface, it is simply assumed that the water concentration in the membrane is in equilibrium with the water in the catalyst layer and varies linearly as a function of liquid saturation in the catalyst layer [18]:

$$C^{eq}_{W,N} = 14C_f + 2.8C_f s \quad \text{if} \quad s > 0 \tag{17}$$

Due to the nature of the membrane, the fluxes of oxygen, water vapour and electronic current in the x direction are set to zero at this interface, where the flux of liquid water and the ionic current are continuous, i.e.

$$\frac{\partial C_{O_2,g}}{\partial x} = 0, \quad \frac{\partial C_{WV,g}}{\partial x} = 0, \quad \frac{\partial p_g}{\partial x} = 0, \quad N_W|_- = N_W|_+, \quad \frac{\partial \phi_s}{\partial x} = 0,$$
$$C_{W,N} = C^{eq}_{W,N}, \quad \sigma_e \frac{\partial \phi_e}{\partial x}\bigg|_- = \sigma_e \frac{\partial \phi_e}{\partial x}\bigg|_+ \tag{18}$$

2.2. Electrochemical kinetics

With respect to the electrochemical oxygen reduction reaction (ORR) at the cathode catalyst layer, the transfer current based on first-order Tafel kinetics can be written as

$$j_c = A_v i_0 \frac{\tilde{C}_{O_2}}{C^{ref}_{O_2}} \exp\left(\frac{\alpha_c F}{RT}\eta_c\right) \tag{19}$$

where $\tilde{C}_{O_2}$ is the surface concentration of oxygen at the active reaction sites (i.e. three-phase interfaces), and η_c represents the cathode overpotential which is calculated by

$$\eta_c = U_0 - \phi_s + \phi_e \tag{20}$$

It has been well documented that the active reaction sites are usually surrounded either by electrolyte films or by liquid water films when a two-phase flow exists. Oxygen in gas pores needs to permeate through these media to the active reaction sites. It is thus necessary to consider the additional mass-transfer resistance of oxygen from gas pores to the actual reaction sites because the diffusivity of oxygen in Nafion or liquid water is quite low. Conventionally, a spherical thin-film agglomerate model

Table 4
Physicochemical properties

Parameters, symbols	Value	Unit	Reference
Porosity of GDL, ε_{gdl}	0.7	–	[19]
Porosity of membrane, ε_{mem}	0.3	–	[19]
Nafion volume fraction in the agglomerate, ε_{agg}	0.5	–	
Volume fraction of solid in CCL, ε_s	0.3	–	
Radius of the agglomerate, R_{agg}	0.6	μm	
Thickness of Nafion film covering the agglomerate, δ_N	20	nm	
Permeability of GDL, $K_{th\text{-}p}$, $K_{in\text{-}p}$	8.69×10^{-12}, 3.0×10^{-12}	m^2, m^2	[2]
Permeability of CL, K	1.0×10^{-14}	m^2	[19]
Permeability of MEM, K	2.0×10^{-18}	m^2	[19]
Electric conductivity of the GDL, $\sigma_{s,thrp}$, $\sigma_{s,inrp}$	100, 2500	Ω^{-1} m^{-1}	[5]
Electric conductivity of CL, σ_s	90	Ω^{-1} m^{-1}	[1]
Diffusivity of O_2 in gas, $D_{O_2,g}$	$1.775 \times 10^{-5}(T/273.15)^{1.823}$	m^2 s^{-1}	[21]
Diffusivity of O_2 in water, $D_{O_2,l}$	3.032×10^{-9}	m^2 s^{-1}	[22]
Diffusivity of O_2 in Nafion, $D_{O_2,N}$	1.844×10^{-10}	m^2 s^{-1}	[22]
Diffusivity of water vapour, $D_{WV,g}$	$2.56 \times 10^{-5}(T/307.15)^{2.334}$	m^2 s^{-1}	[21]
Diffusivity of water in the membrane, $D_{W,N}$	$4.17 \times 10^{-8}\lambda(161\,e^{-\lambda} + 1)\,e^{-2436/T}$	m^2 s^{-1}	[24]
Proton conductivity, σ_e	$(0.5139\lambda - 0.326) \times \exp[1268.0(1.0/303 - 1.0/T)]$	Ω^{-1} m^{-1}	[18]
Water content in membrane, λ	$C_{W,N}/C_f$	–	[18]
Fixed charge sites concentration in membrane, C_f	1200	mol m^{-3}	[18]
Coefficient of electro-osmotic drag of water, n_d	$(2.5/22)\lambda$	–	[18]
Viscosity of gas, liquid phase, μ_g, μ_l	2.03×10^{-5}, 4.05×10^{-4}	kg m^{-1} s^{-1}	[15]
Evaporation rate constant for water, k_e	1	atm^{-1} s^{-1}	[23]
Condensation rate constant for water, k_c	100	s^{-1}	[23]
Henry law constant for oxygen, k_{H,O_2}	$e^{(-666/T+14.1)}/R/T$	–	[22]
The saturation pressure of water vapour, $\log_{10} p^{sat}_{WV}$	$-2.1794 + 0.02953(T-273) - 9.1837 \times 10^{-5}(T-273)^2 + 1.4454 \times 10^{-7}(T-273)^3$	atm	[23]
Thermodynamic voltage of ORR, U_{O_2}	1.21	V	
Pt loading in CCL, m_{Pt}	0.4	mg cm^{-2}	
Specific area in CCL, A_v	$A_0 m_{Pt}/L_{CL}$	m^{-1}	[22]
Exchange current density of ORR, i_0	$10^{(3.507-4001/T)}$	A cm^{-2}	[22]
Transfer coefficient, α_c	1.0	–	[22]
Reference concentration of oxygen, $C^{ref}_{O_2}$	1.2	mol m^{-3}	[22]

[19,20] is employed to capture the influence of the microstructure of catalyst layer, as sketched in Fig. 2. With further taking into account the additional mass-transfer resistance and the interfacial mass transfer resistance, the kinetics of the ORR is expressed as

$$j_c = A_v i_0 \left(\frac{C_{O_2,g}/k_H}{C_{O_2}^{ref}} \right) \exp\left(\frac{\alpha_c F}{RT} \eta_c \right) \xi_1 \xi_2 \xi_3 \quad (21)$$

where k_H, ξ_1, ξ_2 and ξ_3 denote the Henry factor to capture the effect of the dissolving process, the correction factor in view of the transfer resistance in the external Nafion-film, the correction factor in view of the transport resistance in the agglomerate, and the correction factor to capture the effect of the liquid water surrounding agglomerate, respectively. The detailed expressions of the above factors and correlations are listed in Table 2.

3. Results and discussion

The governing equations for the cell geometric dimensions and operating parameters listed in Table 3 subjected to the boundary conditions, along with the constitutive relations shown in Table 1 and the physicochemical properties listed in Table 4, are solved numerically using a self-written code, which was developed based on the SIMPLE algorithm with the finite-volume-method [19,20]. Once the profile of the ionic potential was obtained, the local current density was calculated based on the flux of protons across the CL/PEM interface, and the average current density was then estimated by

$$I_{cell} = \frac{\int_0^{W_c/2+W_r/2} \sigma_e (\partial \phi_e/\partial x)|_{CL/MEM}\, dy}{W_r/2 + W_c/2} = \frac{\iint_{CL} j_c\, dx\, dy}{W_r/2 + W_c/2} \quad (22)$$

In this work, simulations were performed for three different cases. *Case I*: the GDL is treated as an isotropic porous medium and transport coefficients in the GDL are based on its through-plane properties, as sketched in Fig. 1(a). *Case II*: the GDL as an anisotropic structure without deformation, also as sketched in Fig. 1(a). *Case III*: the GDL as an anisotropic structure with deformation.

3.1. Isotropic GDL

The profiles of oxygen concentration, local current density and potentials in the CL along the *y* direction at a given cathode potential of 0.4 V are shown in Fig. 3. Due to the rib coverage effect, oxygen concentration is lower in the region under the rib than that in the region under the channel. Higher oxygen concentration will naturally result in higher cell performance. As shown in Fig. 3(a), as a whole, the current density is greater in the region under the channel than that in the region under the rib. It is interesting to note, however that the highest current density occurs in the location near the interface between the rib and channel (i.e., $x = 0.55$ mm), although the highest oxygen concentration occurs in the location under the middle of the channel (i.e., $x = 1.0$ mm). This can be explained by the fact that the local current density is influenced by both the local oxygen concentration and the cathode overpotential in the CL. As shown in Fig. 3(b), the cathode overpotential decreases gradually from the region under the rib to the region under the channel, as opposed to the variation of the oxygen concentration in the CL. Both variations of the oxygen concentration and cathode overpotential affect the current density distribution. The ultimate profile of current density in the CL is determined by the combined effects of oxygen concentration and overpotential changes. The profiles of the electrical potential and ionic potential in the CL are also displayed in Fig. 3(b). The electric potential gradient is to drive the electric current from all the regions inside the GDL and CL to the rib collector.

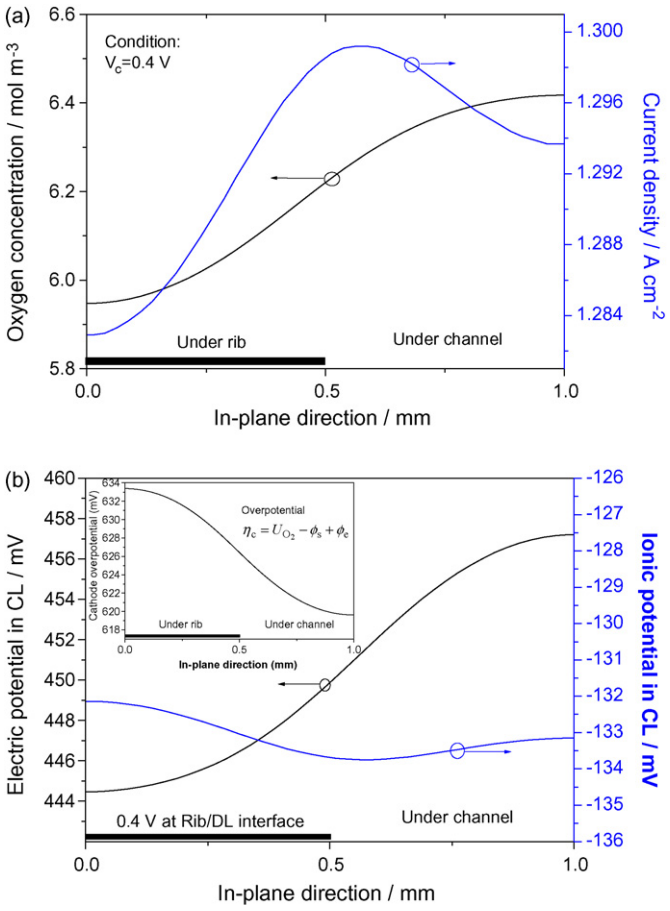

Fig. 3. Variations in oxygen concentration and local current density (a), electrical potential, ionic potential and overpotential in the CL along *y* direction (b) at a given cathode potential of 0.4 V.

Hence, in the regions away from the rib collector, larger potential gradients are required. This is why the electrical potential is always higher in the region under the middle of the channel, as shown in Fig. 3(b). Notice that the difference between the electric potential in the CL and the cathode voltage (i.e., the electrical potential at the ribvertical live GDL interface) represents the ohmic loss due to the resistance of the GDL. With respect to the ionic potential in the CL, it is more uniform along the *y* direction compared with the distribution of the electric potential. With setting a reference value of zero at the vertical live PEM/CL interface, the ionic potential is always negative in the cathode catalyst layer. The absolute value of ionic potential herein denotes the ohmic loss across the membrane as a result of the proton transfer resistance.

The variation in potential along the *x* direction is also displayed in Fig. 4. A relatively large voltage loss, approximate 150 mV, across the membrane can be observed compared with the voltage loss, about 50 mV, across the diffusion layer. This is because the ohmic resistance in the membrane is much higher than that in the GDL.

3.2. Anisotropic GDL without deformation

The GDL exhibits significant anisotropy, leading to different transport properties along the in-plane and through-plane directions. To evaluate the influence of the anisotropic electrical conductivity of the GDL on the distributions of electrical potential and local current density, simulations were conducted by keeping the same through-plane electrical conductivity of the GDL but varying the in-plane electrical conductivity. The profiles of the electrical

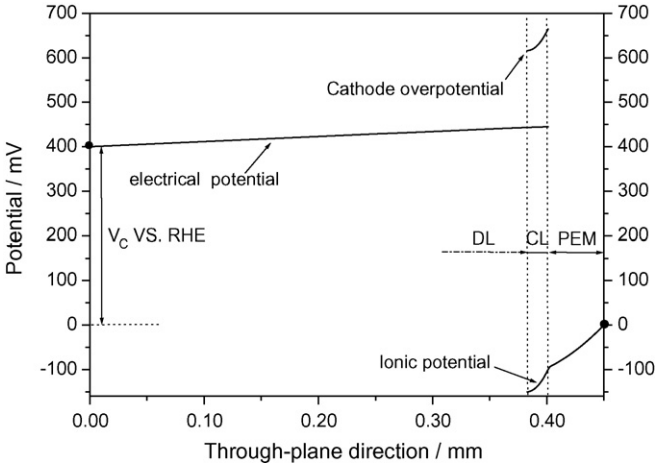

Fig. 4. Variations in electric potential, ionic potential, and overpotential along x direction for given cathode potential of 0.4 V.

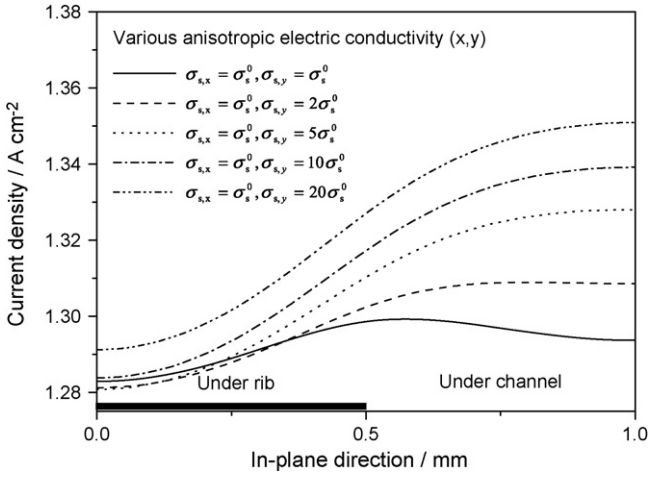

Fig. 6. Variations in local current density along y direction for various in-plane electric conductivities of GDL at given cathode potential of 0.4 V.

potential in the CL along the y direction for various in-plane electrical conductivities are presented in Fig. 5. As the in-plane electrical conductivity is increased, the electron transport along the in-plane direction is enhanced, thereby facilitating the transport of the electrical current from the region under the channel to the rib collector. As shown in Fig. 5, clearly, the electrical potential in the CL decreases significantly as the in-plane electric conductivity is increased, especially that in the region under the channel. In turn, the decrease in the electrical potential in the CL results in an increase in the rate of current generation in the CL. The profiles of the local current density along the y direction for various in-plane electrical conductivities are shown in Fig. 6. As a whole, higher in-plane electric conductivity leads to higher current density. The increase in the current density is more pronounced in the region under the channel than that in the region under the rib, as the electrical potential is more significantly decreased in the region under the channel than that in the region under the rib.

The effective diffusion coefficient of species in a fibrous porous structure also exhibits anisotropic behaviour. For example, in a fibrous porous medium with a porosity of 0.7, the effective factor $f(\varepsilon)$ in Eq. (2) is 0.51 in the through-plane direction, but 0.57 in the in-plane direction. To examine the influence of the anisotropic diffusion coefficients of oxygen in the GDL, an isotropic GDL having the through-plane effective diffusion coefficient is compared with an anisotropic GDL having different diffusion coefficients in the through-plane and in-plane directions. Fig. 7 shows the profiles of local oxygen concentration and local current density along the y direction at a given cathode potential of 0.4 V. Clearly, the oxygen concentration in the CL predicted by the anisotropic transport model is higher than that predicted by the isotropic transport model, especially in the region under the rib. This is primarily due to the fact that the higher in-plane diffusion coefficient benefits the transport of oxygen in the y direction. Consequently, the current density is also higher when the anisotropic transport of oxygen in the GDL is taken into account, as shown in Fig. 7.

The fuel cell performance predicted, by the isotropic and anisotropic transport models is compared in Fig. 8. At low-current densities (<0.3 A cm^{-2}), the cell performance predicted by the two models is almost the same, as both the ohmic and the concentration polarization at low-current densities are negligible. With increase in cell current density, a voltage difference between the two curves can be observed and becomes significant at large current densities. For example, at a current density of 1.0 A cm^{-2}, the voltage predicted by the anisotropic transport model is about 25 mV higher than that predicted by the isotropic transport model. The data in Fig. 8 also show that the maximum power density predicted by

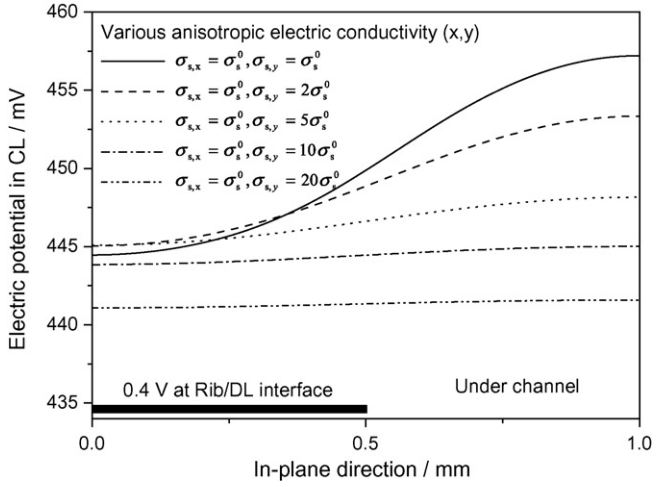

Fig. 5. Variations in electrical potential in CL along y direction for various in-plane electric conductivities of GDL at given cathode potential of 0.4 V.

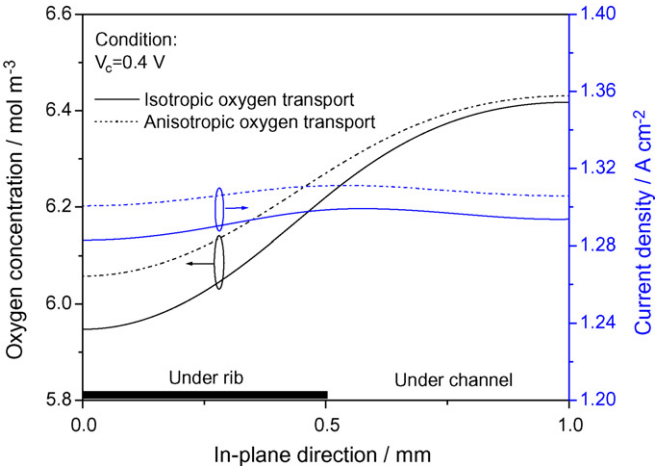

Fig. 7. Variations in oxygen concentration and current density in CL along y direction for both isotropic transport and anisotropic GDLs.

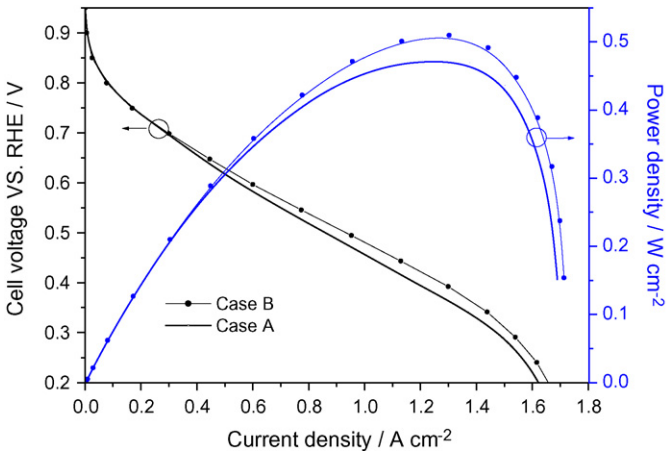

Fig. 8. Comparison in fuel cell performance simulated with isotropic transport model (case A) and anisotropic transport model (case B).

the anisotropic model is about 9% higher than that by the isotropic model.

3.3. Anisotropic GDL with deformation

Deformation of the GDL is usually encountered in a fuel cell when all the cell components are assembled. Due to the deformation, the thickness and the physical properties of the GDL and the interfacial contact resistance are all changed. For the purpose of modelling, the set of correlations given in Ref. [5], as listed in Table 1, is simply employed to capture the effect of the GDL deformation. It is particularly worth mentioning that the GDL deformation is not homogeneous. The parts of the GDL situated under the rib are more significantly compressed than those under the channel. Such inhomogeneous deformation may cause significant variation in the local physical properties of the GDL along the *y* direction, thereby influencing local current densities.

To examine the effects of GDL deformation on the reactant, potentials, and current distributions, as well as on the overall cell performance, the following three cases are compared: (a) isotropic GDL without deformation, (b) anisotropic GDL without deformation and (c) anisotropic GDL with deformation.

The distribution of oxygen concentration in the GDL and CL for the three cases are given in Fig. 9. The simulations are performed at the same current density of 1.1 A cm^{-2}. A comparison between Fig. 9(a) and (b) shows that the oxygen concentration in the region under the rib is relatively higher for the anisotropic GDL than that for the isotropic GDL. This is due to the fact that the large in-plane effective diffusivity of oxygen in the anisotropic GDL leads to a higher rate of oxygen transport along the in-plane direction. When the GDL is under inhomogeneous deformation, the porosity of GDL in the region under the rib is greatly reduced, lowering the effective diffusivity of oxygen in both in-plane and through-plane directions. As a result, the oxygen concentration is very low in the region under the rib, as shown in Fig. 9(c). The variations in oxygen concentration in the CL along the *y* direction are presented in Fig. 10. With taking the GDL deformation into account, the oxygen concentration is greatly decreased. Compared with the case for an anisotropic GDL without deformation, the oxygen concentration in the region under the rib is decreased by 50% when the effect of GDL deformation is taken into account. By contrast, a only 10% decrease in oxygen concentration is observed in the region under the channel, as the GDL deformation is relatively smaller in the region under the channel. Usually, at a given cell current density a lower concentration of oxygen in the CL results in a higher concentration polarization. As clearly shown in Fig. 11, the cathode overpotential is much higher when the GDL deformation is considered. In addition, the profile of cathode overpotential becomes more uneven because of the inhomogeneous deformation of the GDL.

The distributions of electrical potential at a cell current density of 1.1 A cm^{-2} are presented in Fig. 12. For an isotropic GDL

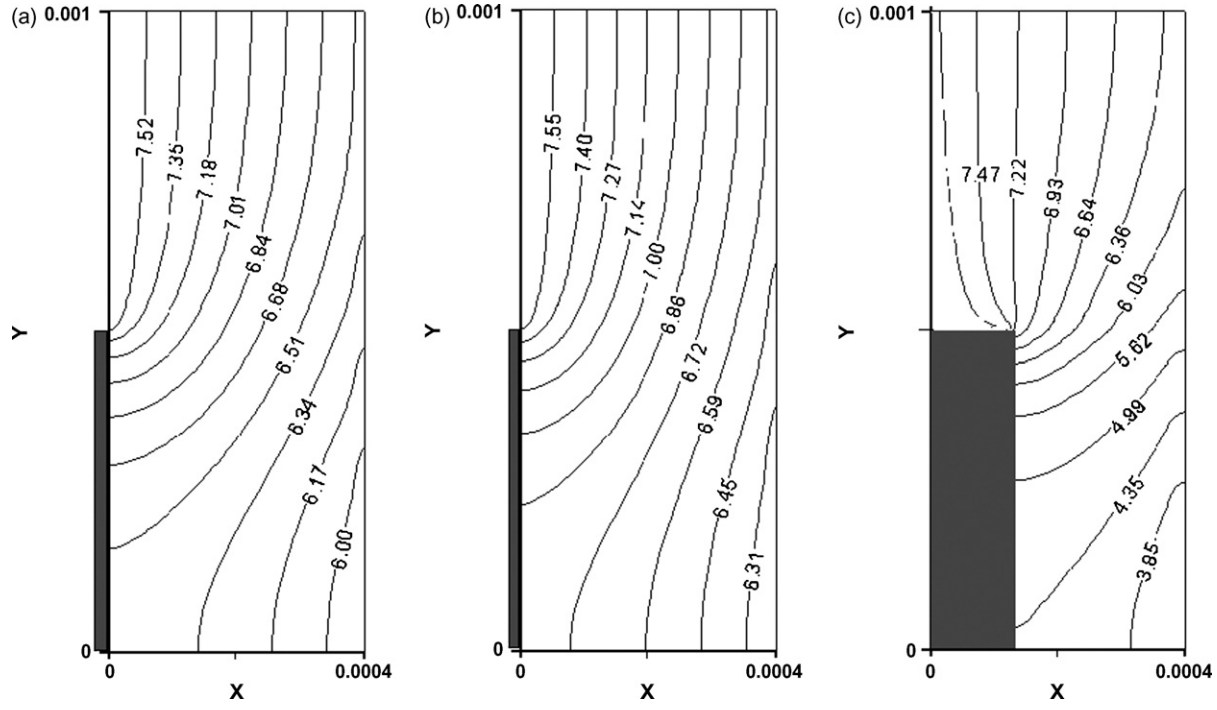

Fig. 9. Distribution of oxygen concentration in GDL and CL for (a) isotropic GDL without deformation, (b) anisotropic GDL without deformation, and (c) anisotropic GDL with deformation.

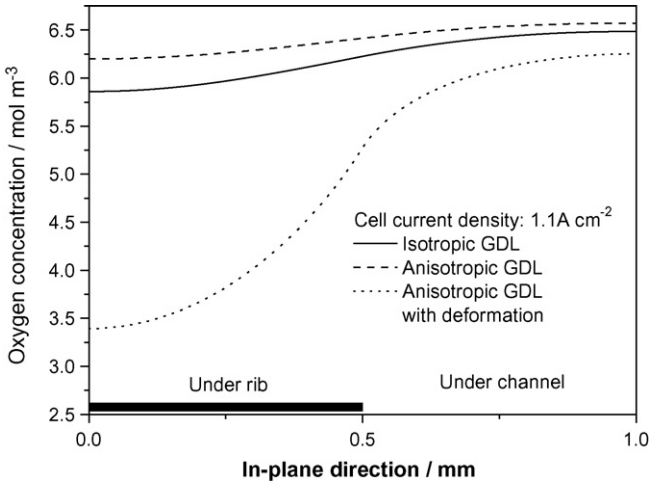

Fig. 10. Profiles of local oxygen concentration in CL along *y* direction.

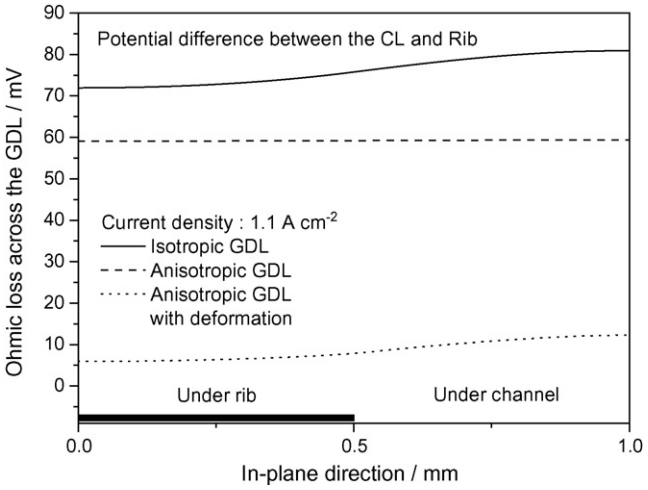

Fig. 13. Electric potential difference between CL and rib.

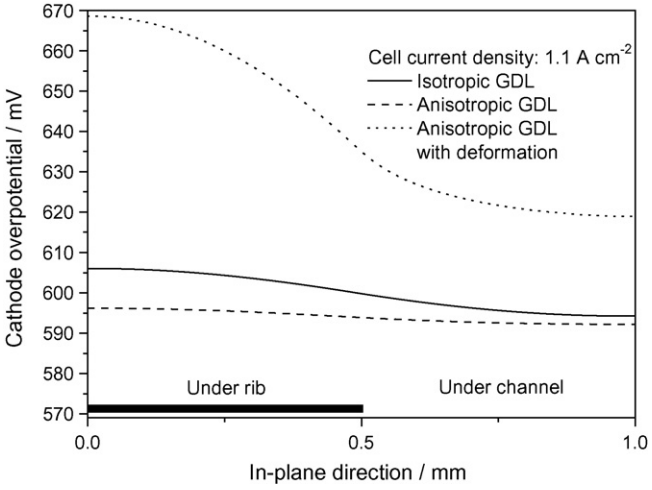

Fig. 11. Variations in cathode overpotential along *y* direction.

without deformation, electron transport in the in-plane direction requires a higher potential gradient because of the lower electronic conductivity, as shown in Fig. 12(a). By contrast, the electronic potential for an anisotropic GDL without deformation displays almost one-dimension behaviour with little variation in the in-plane direction due to the large in-plane electrical conductivity, as shown in Fig. 12(b). When the GDL is under inhomogeneous deformation, much higher electronic conductivities can be achieved compared with the original value, especially in the region under the rib. As a result, electron transport requires much smaller potential gradients as can be seen in Fig. 12(c). The electronic potential drops from the CL to the rib collector are also plotted in Fig. 13. Clearly, the largest fall in electronic potential across the GDL is only about 12 mV for the case with the GDL deformation, which is much smaller than the values of 60 mV and 80 mV for an anisotropic GDL without deformation and an isotropic GDL, respectively.

Although GDL deformation results in an increase in the concentration polarization as the result of the increased mass-transfer resistance of oxygen, it also contributes to the decrease in the ohmic loss due to the decreased electrical resistance of the GDL

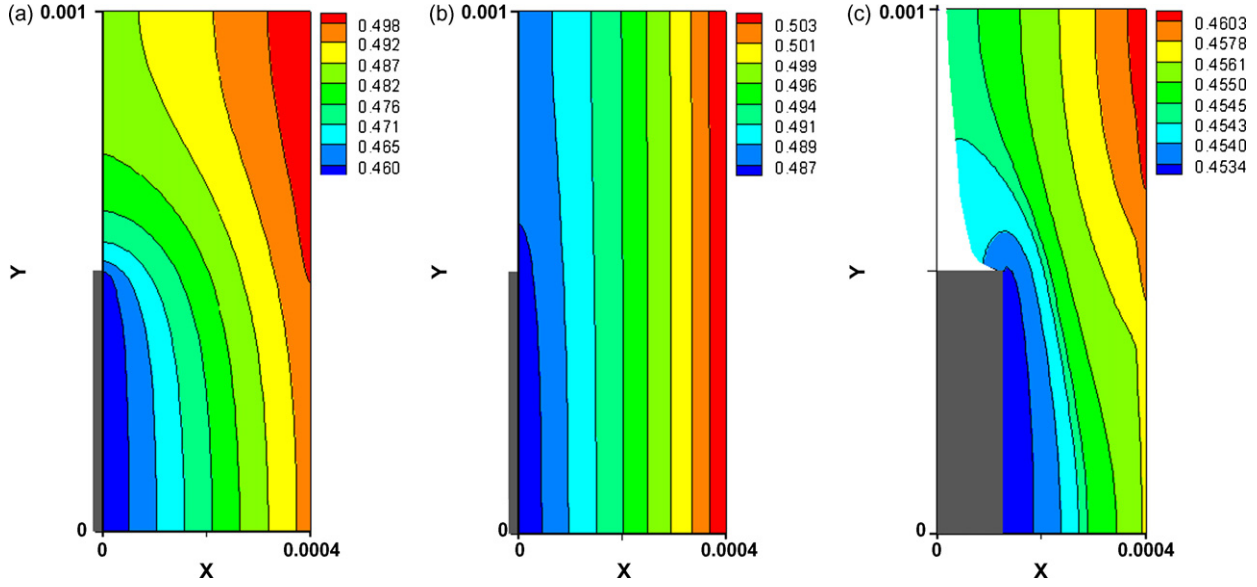

Fig. 12. Distributions of electric potential in GDL and CL at cell current density of 1.1 A cm^{-2} for (a) isotropic GDL without deformation, (b) anisotropic GDL without deformation, and (c) anisotropic GDL with deformation.

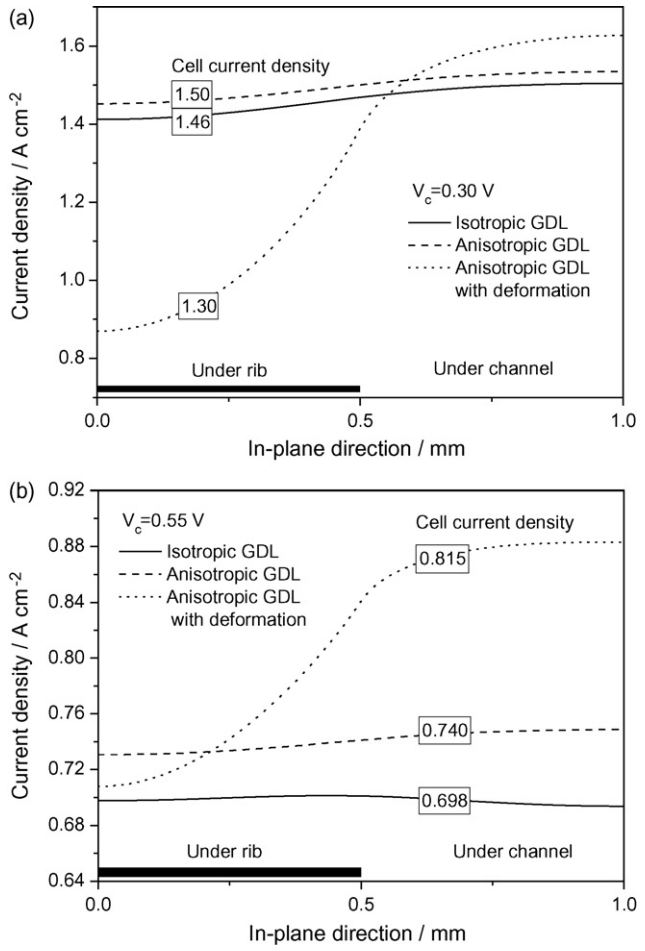

Fig. 14. Profiles of local current density for different cathode potentials of (a) 0.3 V and (b) 0.55 V.

and the interfacial contact resistance. Cell performance is finally determined by taking into account both the adverse effect and the favourable effect. Fig. 14 shows the current density profiles at given cathode potentials of 0.3 and 0.55 V. Normally, at the low-cathode potential of 0.3 V, cell performance tends to be dominated by the concentration polarization as a result of the mass-transfer resistance in the GDL. As shown in Fig. 14(a), the averaged current density for the anisotropic GDL with deformation is about 13% lower than that for the anisotropic GDL without deformation. This is because severe concentration polarization results from the GDL deformation as discussed earlier. Additionally, the profile of local current density becomes more uneven for an anisotropic GDL with deformation due to the inhomogeneous properties of the GDL. At a moderate cathode potential of 0.55 V, however, the ohmic polarization gradually becomes dominant, while the effect of concentration polarization fades. Although GDL deformation somewhat increases the resistance of oxygen transfer, resulting in a slight increase in the concentration polarization, the significant decrease in the electric resistance of the GDL and interfacial contact resistance greatly lowers the ohmic loss. Consequently, the overall current density for an anisotropic GDL with deformation shows a 10% increase compared with that for anisotropic GDL without deformation, as shown in Fig. 14(b).

A comparisons of cell performance for the three cases is given in Fig. 15. Clearly, an anisotropic GDL with deformation results in the smallest limiting current density because of the largest mass-transfer resistance of oxygen in the GDL. It is found however, an anisotropic GDL with deformation and an anisotropic GDL without deformation show approximately the same maximum power density. More importantly, an anisotropic GDL with deformation exhibits a better performance current densities that range from 0.3

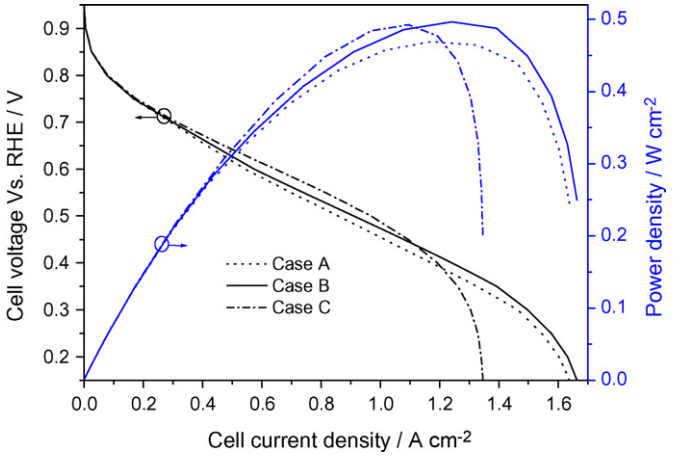

Fig. 15. Comparison in cell performance (case A: isotropic GDL without deformation; case B: anisotropic GDL without deformation; case C: anisotropic GDL with deformation).

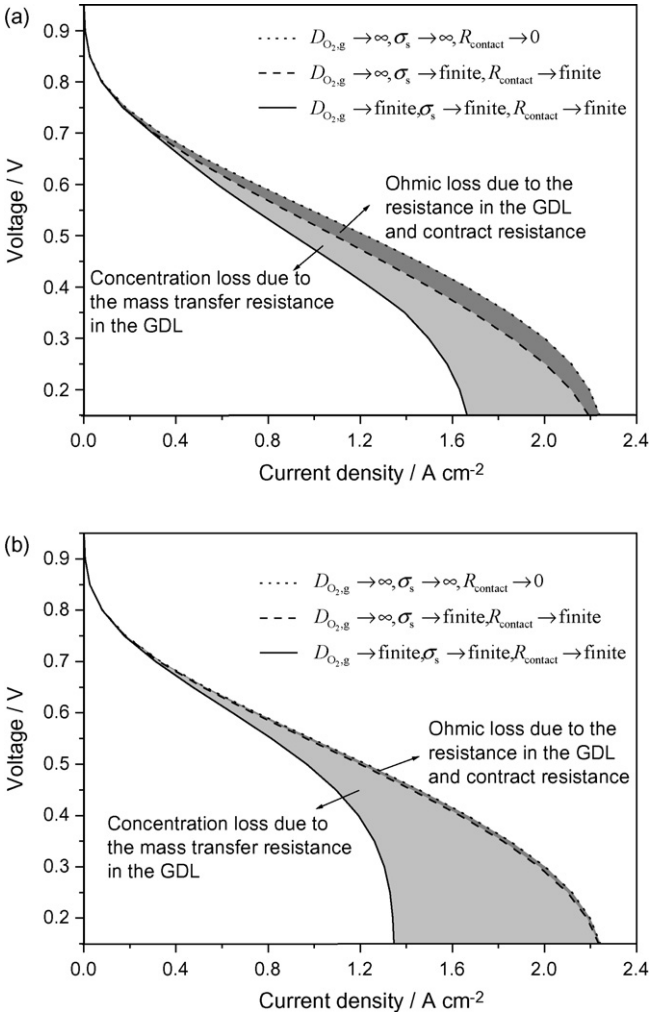

Fig. 16. Ohmic loss and concentration loss for (a) anisotropic GDL without deformation and (b) anisotropic GDL with deformation.

to 1.1 A cm^{-2}. It is well accepted that the cell practically tends to be operated at moderate or relatively low-current densities in order to provide a relatively high-cell voltage and efficiency. In this way, the case for the anisotropic GDL with deformation actually shows better performance than that without deformation.

The concentration loss due to the mass-transfer resistance of oxygen in the GDL and the ohmic loss due to the electrical resistance of the GDL and the interfacial contact resistance are compared in Fig. 16 for an anisotropic GDL without and with deformation. Clearly, at a given current density, the concentration loss is higher for the anisotropic GDL with deformation. The ohmic loss is virtually negligible from anisotropic GDL with deformation, as shown in Fig. 16(b), but it becomes large for the anisotropic GDL without deformation, as shown in Fig. 16(a). Technically speaking, the results indicate that a potentially high performance can be achieved for an anisotropic GDL with deformation by enhancing oxygen transport in the GDL. Two points must be highlighted. First, although GDL deformation contributes to the decrease in the resistance of the GDL and interfacial contact resistance, this effect is usually limited. Second, although GDL deformation leads to an increase in the mass transfer resistance, the mass-transfer of oxygen in the GDL may be enhanced by using a new flow-field and other techniques. Practically, an optimum deformation should be achieved in order to maintain high and reliable cell performance.

4. Conclusion

A two-dimensional model for predicting coupled electron and two-phase mass transport processes in an anisotropic GDL of a PEMFC is presented in this work. The feature of this model is that it can be used to assess the impacts of the GDL anisotropic transport properties associated with carbon fibres and caused by GDL deformation. The numerical results indicate that for the GDLs that are made of carbon fibres the anisotropic transport properties, particularly electrical conductivity, significantly influence the distributions of local electrical potential and local current density, as well as the overall cell performance. The numerical results also show that the deformation of the GDL also plays an important role in determining the performance of a PEMFC. Due to the inhomogeneous GDL deformation, local transport properties in the GDL and the interfacial contact resistance are all significantly changed, which results in more uneven distributions of reactant concentration and current density. It is found that GDL deformation significantly reduces the limiting current density of the cell because of the increased mass-transfer resistance in the deformed GDL, although the ohmic loss becomes smaller as a result of decreased contact resistance after deformation. Practically, an optimum deformation should be achieved such that a higher limiting current density and lower ohmic resistance can be maintained.

Acknowledgments

The work described in this paper was supported by a grant from the Research Grants Council of the Hong Kong Special Administrative Region, China (project no. 622807) and by the Joint Research Fund for Hong Kong and Macao Young Scholars (project no. 50629601).

References

[1] T.H. Zhou, H.T. Liu, J. Power Sources 162 (2006) 444–453.
[2] U. Pasaogullari, P.P. Mukherjee, C.Y. Wang, K.S. Chen, J. Electrochem. Soc. 154 (2007) B823–B834.
[3] J.G. Pharoah, K. Karan, W. Sun, J. Power Sources 161 (2006) 214–224.
[4] H. Meng, J. Power Sources 161 (2006) 466–469.
[5] T. Hottinen, O. Himanen, S. Karvonen, I. Nitta, J. Power Sources 171 (2007) 113–121.
[6] P. Zhou, C.W. Wu, G.J. Ma, J. Power Sources 159 (2006) 1115–1122.
[7] L. Zhang, Y. Liu, H. Song, S. Wang, Y. Zhou, S. Hu, J. Power Sources 162 (2006) 1165–1171.
[8] V. Mishra, F. Yang, R. Pitchumani, Trans. ASME J. Fuel Cell Sci. Technol. 1 (2004) 1–9.
[9] J.B. Ge, A. Higier, H.T. Liu, J. Power Sources 159 (2006) 922–927.
[10] W.R. Chang, J.J. Hwang, F.B. Weng, S.H. Chan, J. Power Sources 166 (2007) 149–154.
[11] P. Zhou, C.W. Wu, J. Power Sources 170 (2007) 93–100.
[12] P. Zhou, C.W. Wu, G.J. Ma, J. Power Sources 163 (2007) 874–881.
[13] T. Hottimen, O. Himanen, S. Karvonen, I. Nitta, J. Power Sources 171 (2007) 26–36.
[14] T. Hottimen, O. Himanen, Electrochem. Commun. 9 (2007) 1047–1052.
[15] J.H. Nam, M. Kaviany, Int. J. Heat Mass Transf. 46 (2003) 4595–4611.
[16] M.M. Tomadakis, S.V. Sotirchos, AIChE J. 39 (1993) 397–403.
[17] W.W. Yang, T.S. Zhao, J. Power Sources 174 (2007) 136–147.
[18] G.Y. Lin, T.V. Nguyen, J. Electrochem. Soc. 153 (2006) A372–A382.
[19] W.W. Yang, T.S. Zhao, Electrochim. Acta 52 (2007) 6125–6140.
[20] W.W. Yang, T.S. Zhao, C. Xu, Electrochim. Acta 53 (2007) 853–862.
[21] Z.H. Wang, C.Y. Wang, J. Electrochem. Soc. 150 (2003) A508–A519.
[22] D. Song, Q. Wang, Z. Liu, T. Navessin, M. Eikerling, S. Holdcroft, J. Power Sources 126 (2004) 104–111.
[23] A. Kazim, H.T. Liu, P. Forges, J. Appl. Electrochem. 29 (1999) 1409–1414.
[24] H. Meng, C.Y. Wang, J. Electrochem. Soc. 151 (2004) A358–A367.